

Cite this: *J. Mater. Chem. C*, 2021,
9, 5267

Ferroelectric state and polarization switching behaviour of ultrafine BaTiO₃ nanoparticles with large-scale size uniformity†

Yanan Hao,^{ab} Zunpeng Feng,^a Soham Banerjee,^c Xiaohui Wang,^{*b}
Simon J. L. Billinge,^{*cd} Jiesu Wang,^e Kuijuan Jin,^e Ke Bi^{ib} ^{*a} and Longtu Li^b

BaTiO₃ (BTO) nanoparticles (NPs) with controlled particle sizes of 2.8, 4.5 and 8.1 nm and large-scale size uniformity are fabricated. The structure and polarization switching behaviour of the 4.5 nm BTO NPs are investigated. Structural analysis using the atomic pair distribution function (PDF) technique confirms that the particles are non-centrosymmetric at room temperature, and reveals that the ferroelectric distortions are spatially coherent. With increasing temperature, declined ferroelectric features and responses are observed by Raman scattering and second harmonic generation (SHG), suggesting a diffuse phase transition. After self-assembly into compact thin films, selectively written and read electric polarization of the nanocrystals show direct evidence for the presence of ferroelectricity, demonstrating that the local spatial coherent asymmetric nanoparticles with detectable Ti distortion can lead to sufficient macroscopic polarization in the 4.5 nm BTO NP aggregate. The results indicate that these ultrafine ferroelectric NPs are promising candidate materials for the fabrication of high-density ferroelectric memory devices.

Received 22nd December 2020,
Accepted 16th March 2021

DOI: 10.1039/d0tc05975g

rsc.li/materials-c

1. Introduction

Ferroelectric materials, which are widely used in capacitors,^{1,2} memory devices,³ and energy storage applications,^{4–6} have played an important role in the rapid development of modern electronics in the past few decades.^{7–13} The investigation of polarization switching behaviour and underlying physics for ultrafine ferroelectric materials enables an explosive increase in the capacity of microelectronics. Since ferroelectricity often guides the design and fabrication of such devices, the recent size reduction constraint in ferroelectric microelectronics revives an old question concerning the possible existence of critical size below which the ferroelectricity disappears.^{7,14–18}

One of the most widely studied ferroelectric materials, BTO, crystallizes in a typical perovskite structure which is cubic (*Pm3m*) above the Curie temperature, and undergoes several lowering symmetry phase transitions from tetragonal (*P4mm*) to orthorhombic (*Amm2*) to rhombohedral (*R3m*), as the temperature is reduced. Ferroelectricity in BTO originates from the displacement of Ti atoms inside the perovskite octahedron for the non-centrosymmetric phases. With decreasing crystallite size, previous reports showed a progressive reduction of tetragonal ferroelectric distortion, Curie temperature and dielectric constant in bulk BTO.¹⁵

For BTO NPs, the structural evolution becomes more complex and different synthesis techniques yield considerably different nanostructures.^{7,19,20} For example, monodomain² and multiphase coexistence states²¹ were illustrated in sub-10 nm particles, respectively. In general, due to variability in ligand-dependent surface relaxation,^{22–24} depolarization fields,^{25,26} internal stresses^{27,28} and other influencing factors,^{15,29} nano-sized BTO shows declined overall structural coherence, with a more cubic-like structure identified by bulk probes. The PDF pattern of ~90 Å BTO NPs reported by Rabuffetti *et al.* vanished after 45 Å.³⁰ Similarly, Petkov *et al.* found that the PDF of 5 nm BTO NPs became featureless after 2 nm.³¹ Although local probes have identified distortions with large Ti displacements which are comparable, or even higher than the values reported for the bulk materials, most studies demonstrate that driven by the surface-induced phenomena and depolarization effects, the

^a State Key Laboratory of Information Photonics and Optical Communications, School of Science, Beijing University of Posts and Telecommunications, Beijing 100876, China. E-mail: bike@bupt.edu.cn

^b State Key Laboratory of New Ceramics and Fine Processing, School of Materials Science and Engineering, Tsinghua University, Beijing 100084, China. E-mail: wxh@tsinghua.edu.cn

^c Applied Physics and Applied Mathematics Departments, Columbia University, New York, NY 10027, USA. E-mail: sb2896@columbia.edu

^d Condensed Matter Physics and Materials Science Department, Brookhaven National Laboratory, Upton, NY 11973, USA

^e Beijing National Laboratory for Condensed Matter Physics, Institute of Physics, Chinese Academy of Sciences, Beijing 100190, China

† Electronic supplementary information (ESI) available. See DOI: 10.1039/d0tc05975g

enhanced local ferroelectric distortions always coincide with a declined overall polar distortion.^{29–32} This phenomenon is known to influence the structure-related macroscopic ferroelectric response. However, the connection between macroscopic polarization, and reduced structural coherence of the ferroelectric distortion in BTO remains unsettled. It is generally accepted that long-range cooperative structural distortions of the local atomic environments are required for a thermodynamically stable non-centrosymmetric phase and ferroelectric behaviour in nanostructured BTO.^{15,30,31} Despite significant progress in this area, the exploration of a ferroelectric critical size, and the characterization of macroscopic polarization response still remains a challenge, due to the difficulty in synthesizing ultrafine, monodisperse BTO NPs, and characterizing nanoparticle assemblies at the nanoscale.

In this work, local structures as well as macroscopic ferroelectric polarization are examined on the free-standing BTO NPs (4.5 nm) and their self-assembled thin films. We ensure that the nanocrystal thin films maintain a small crystal size by fabricating them at low temperatures (~ 160 °C); this enables direct detection of the ferroelectric response from the nanoparticles by multiple thin film characterization methods. The results provide a detailed crystal structure analysis, and the corresponding ferroelectric behaviours of BTO NPs assemblies at the smallest accessible length scales. Unlike other structural studies of sub 10 nm BTO that report a room temperature cubic structure, PDF analysis reveals that these BTO NPs, synthesized by the TEG-sol method,³³ have a non-centrosymmetric crystal structure with a high structural coherence length, under ambient conditions. With increasing temperature, the Raman bands shift gradually, and the bands originated from the tetragonal ferroelectric phase stabilize even at 400 °C. This reveals a considerably diffuse phase transition process over a wide temperature range. Accordingly, the SHG response that relates to the non-centrosymmetrical phase structures also declines with increasing temperature. Due to the significant structural coherence and large magnitude of the Ti off-centering displacements, these nanoparticles exhibit detectable ferroelectric properties which can be polarized, and switched selectively as coarse particles under an external electric field. Ferroelectric behaviour of these 4.5 nm BTO NPs assemblies was characterized by Piezoelectric Force Microscopy (PFM). The results described here confirm the ferroelectricity of these sub 10 nm BTO NPs, which not only provides a basis for fabricating nonvolatile memory devices and high-performance dielectrics, but also extends the application of ferroelectric nanocrystals to a variety of emerging fields, for example, printed electronics, energy storage, nanogenerators, and more.³³

2. Experimental procedure

2.1 Sample preparation

The 2.8, 4.5 and 8.1 nm BaTiO₃ powders and nanocrystal sols were prepared by controlled hydrolysis of Ti(OC₄H₉)₄ in triethylene glycol (TEG), which has been reported earlier.³⁴ The BaTiO₃ nanocrystal film that was used for SHG and PFM characterization was spin coated using the highly stable BaTiO₃

sol on Pt-coated SiO₂/Si substrate and subsequently dried at 160 °C for solvent evaporation. Then the samples were characterized without further heat treatment. A multiple spin coating process was utilized to get the different film thicknesses.

2.2 PDF

Total scattering PDF experiments were carried out at the 28-ID-II (XPD) beamline (NSLS-II; Brookhaven National Lab) using the rapid acquisition PDF method (RAPDF).³⁵ BaTiO₃ nanopowders were loaded in 1.02 mm (OD) polyimide capillaries and a 2D detector was placed 205.312 mm behind the samples in a Debye-Scherrer geometry. The incident wavelength of the X-rays was $\lambda = 0.184094$ Å. The sample-detector distance, 2θ range, and detector misorientations were calibrated by measuring a crystalline Ni powder directly prior to data collection for the nanoparticulate sample, with the experimental geometry parameters refined using the PyFAI program.³⁶ Masks were created to remove outlier pixels and the beam stop shadow using an automasking procedure³⁷ and applied to the images before azimuthal integration. Standardized corrections are then made to the data and normalizations carried out to obtain the total scattering structure function, $F(Q)$, which is then Fourier transformed to obtain the PDF, using PDFgetX3³⁸ within xPDFsuite.³⁹ The maximum range of data used in the Fourier transform (Q_{\max}), where $Q = 4\pi\sin\theta/\lambda$ is the magnitude of the momentum best trade off between statistical noise and resolution.

The experimental PDF, denoted $G(r)$, is the truncated Fourier transform of the total scattering structure function, $F(Q) = Q[S(Q) - 1]$.⁴⁰

$$G(r) = \frac{2}{\pi} \int_{Q_{\min}}^{Q_{\max}} F(Q) \sin(Qr) dQ \quad (1)$$

where Q is the magnitude of the scattering momentum. The structure function, $S(Q)$, is extracted from the Bragg and diffuse components of X-ray, neutron or electron powder diffraction intensity. For elastic scattering, $Q = 4\pi\sin(\theta)/\lambda$, where λ is the scattering wavelength and 2θ is the scattering angle. In practice, values of Q_{\min} and Q_{\max} are determined by the experimental setup and Q_{\max} is often reduced below the experimental maximum to eliminate noisy data from the PDF since the signal to noise ratio becomes unfavorable in the high- Q region.

The PDF gives the scaled probability of finding two atoms in a material a distance r apart and is related to the density of atom pairs in the material.⁴¹ For a macroscopic scatterer, $G(r)$ can be calculated from a known structure model according to

$$G(r) = 4\pi r [\rho(r) - \rho_0] \quad (2)$$

$$\rho(r) = \frac{1}{4\pi r^2 N} \sum_i \sum_{j \neq i} \frac{b_i b_j}{\langle b \rangle^2} \delta(r - r_{ij}) \quad (3)$$

here, ρ_0 is the atomic number density of the material and $\rho(r)$ is the atomic pair density, which is the mean weighted density of neighbor atoms at distance r from an atom at the origin. The sums in $\rho(r)$ run over all atoms in the sample, b_i is the scattering factor of atom i , $\langle b \rangle$ is the average scattering factor and r_{ij} is the distance between atoms i and j .

In practice, we use eqn (2) and (3) to fit the PDF generated from a structure model to a PDF determined from an experiment. For this purpose, the delta functions in eqn (3) are Gaussian-broadened and the equation is modified to account for experimental effects. PDF modeling, where it is carried out, is performed by adjusting the parameters of the structure model, such as the lattice constants, atom positions and anisotropic atomic displacement parameters, to maximize the agreement between the theoretical and experimental PDFs.

2.3 Other characterizations

Temperature-dependent Raman spectra were recorded in the 100–1000 cm^{-1} wavenumber range using a confocal microscopic Raman spectrometer (HR800, Horiba JobinYvon, France) with a 633 nm wavelength laser radiation and a temperature control system (Linksys32, T95-System, Guildford, UK). The HR-TEM image of the BaTiO_3 nanoparticles was obtained by using a TEM (JEM-2100, JEOL Ltd, Tokyo, Japan) at an accelerating voltage of 200 kV. The surface and cross-sectional morphology of the nanocrystal thin film were observed using a scanning electron microscope (SEM; JSM-7001F, JEOL Ltd, Tokyo, Japan) operated at 20 kV. Optical SHG measurement was carried out in the back-scattering geometry (shown in Fig. 6) using a Ti:Sapphire laser. The laser has a central wavelength of 800 nm, pulse duration of 120 fs, repetition rate of 82 MHz and an average power of 200 mW. The film sample was fixed on the temperature control stage of Linksys32 system by silver paste. PFM imaging of the BaTiO_3 nanocrystal film was performed using a piezoelectric force microscopy (Cypher S, Asylum Research, Santa Barbara, USA) with conductive, platinum coated tips. For the polarization switching image, firstly a graphic pattern was written on the film in the contact mode with a high DC voltage of ± 40 V (writing mode). Then the phase signals were collected at a scanning frequency of 1 Hz and a DC voltage of +5 V (reading mode). The PDF, Raman scattering, SHG and PFM characterizations are all performed on the 4.5 nm BTO NPs.

3. Results and discussion

3.1 Morphology

The fabricated BTO NPs have large-scale size uniformity. Due to the TEG-sol based method, the reaction product maintains a

transparent sol state with a limited crystal size. When the sol state is broken, large crystals are obtained. The high-resolution transmission electron microscope (HR-TEM) images that inserted present clear lattice fringes but blurry edge, which indicates that the nanocrystals are coated with an organic layer. This organic coating is the basis for the sol stability. Therefore, the BTO NPs separated from the sol have large-scale size uniformity. Tuning the solution composition can slightly control the average size of the nanocrystals in the sol. Fig. 1 shows the as-prepared BTO NPs with crystal size of (a) 2.8 ± 1.0 nm, (b) 4.5 ± 1.5 nm and (c) 8.1 ± 3.0 nm. Obviously, the size distribution is quite narrow and no abnormal large particles are observed. The large-scale size uniformity of the nanocrystals ensures that the ferroelectric response originates from the ultrafine NPs.

3.2 PDF analysis

Total scattering methods, including atomic pair distribution function (PDF) analysis, are ideal for quantitative and reliable structural analysis of ultra-small nanoparticles.^{31,32,42–45} Here we characterize the 4.5 nm BaTiO_3 NPs using PDF to investigate whether the observed ferroelectric properties of the particles, assembled into thin films, have an atomic scale origin. For a material to exhibit a ferroelectric response, there must exist a net dipole moment, or polarization, and this polarization must be switchable under an applied electric field. In BTO, ferroelectric dipoles emerge from displacements of Ti atoms off the center of TiO_6 octahedra. For bulk crystals, displacive models^{46,47} are commonly used to explain the phase transitions where Ti off-centering occurs along different crystallographic directions as the temperature is reduced below 393 K, above which the material is paraelectric and Ti atoms are centered.^{48,49}

In this study, we aim to determine if there is any evidence of Ti off-centering at room temperature in these ultra-small BTO NPs, by testing the three noncentrosymmetric ferroelectric phases found in the bulk, along with the high temperature centrosymmetric paraelectric phase. Fig. S1 (ESI[†]) shows the measured PDFs for the BTO NPs with crystal sizes approximately of 3 nm and 5 nm and their selected area diffraction patterns, respectively. Marked using the red hexagon, the refined crystal size of the NPs coincides well with the TEM

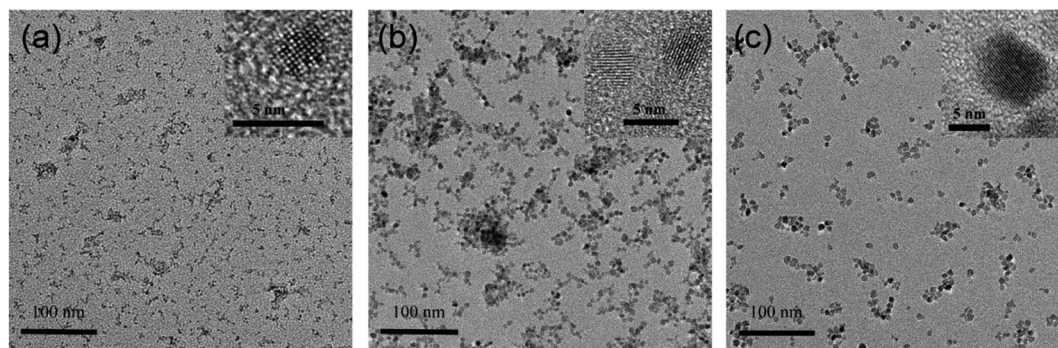


Fig. 1 Large-scale morphology of the BTO NPs with crystal size of (a) 2.8 ± 1.0 nm; (b) 4.5 ± 1.5 nm; (c) 8.1 ± 3.0 nm.

observation. And the diffraction pattern reveals good crystallinity of the nanocrystals. For convenience, we name the nanoparticles with their average size calculated from the TEM observation. Fig. S2 (ESI†) presents the measured PDFs, along with the four candidate BTO crystallographic phases fit to the experimental PDF for the 4.5 nm nanocrystals. As shown, all the candidate models yield refined crystallite sizes in decent agreement with the TEM determined particle size (4.5 ± 1.5 nm). These particles appear to be monodomain, with limited evidence of reduced ferroelectric distortions. The result reveals that these particles have high structural coherence of the ferroelectric distortions.

We first fit the data for the 4.5 nm BTO NPs with the high temperature cubic perovskite structure in the $Pm\bar{3}m$ space group, containing a Ti-atom at the $(\frac{1}{2}, \frac{1}{2}, \frac{1}{2})$ inversion center in the asymmetric unit cell. The experimental PDF is fit over a wide r -range, $1.5 < r < 60$ Å, using an attenuated crystal (AC) approximation that also allows us to extract an average crystallite size for the nanoparticles. We can see from the fit in Fig. 2a and the refined structural parameters in Table 1 that the centrosymmetric model ($Pm\bar{3}m$) appears to describe most of the signal in the measured PDF, and the goodness-of-fit, $R_w = 0.163$, is comparable to, or better than what is reported in PDF studies of similarly sized BTO NPs.^{29,30,32,50,51} However, rather noticeably, the refined isotropic atomic displacement parameter (ADPs) for the Ti atomic site in the centrosymmetric cubic model ($Pm\bar{3}m$) is typically large for well-ordered NPs of

this size, with $Ti-U_{iso} = 0.019$ Å². Constraining the lattice constants by tetragonal symmetry ($P4/mmm$), while keeping the Ti-atom position fixed at the inversion center also does little to improve the goodness-of-fit or ADP values.

To test the three noncentrosymmetric ferroelectric phases of BTO we allow for Ti atom displacements along the (001), (011), and (111) directions, in the tetragonal ($P4mm$), orthorhombic ($Amm2$) and rhombohedral ($R3m$) space group settings, respectively. Reducing symmetry and testing distortions hierarchically, while ensuring that initial values for structural variables are kept consistently independent of the symmetry constraints, is done conveniently in PDFgui.⁵² The refinements of the noncentrosymmetric models are shown in Fig. 2b–d, with the different displacement modes illustrated in the insets. By visual inspection alone, the fits and fit residuals appear similar. In Fig. 3 we focus on two of the key fit parameters, the agreement factor (R_w) and the refined atomic displacement parameter (U_{iso}) for the Ti atomic site. There are fairly significant improvements in agreement for the non-centrosymmetric (Fig. 3a) models compared to the centrosymmetric one (Fig. 3b), but even more convincingly, the change in ADP values for off-centered Ti atoms (Fig. 3d) is very large, reducing by a factor of ~ 2 for all three of the noncentrosymmetric models. Refined ADPs for O atoms, given in Table 1 do not differ appreciably between any of the models tested. Together, this provides strong evidence that the 4.5 nm BaTiO₃ NPs studied here are non-centrosymmetric with Ti moving off the center of inversion symmetry. With this analysis it is not possible to differentiate

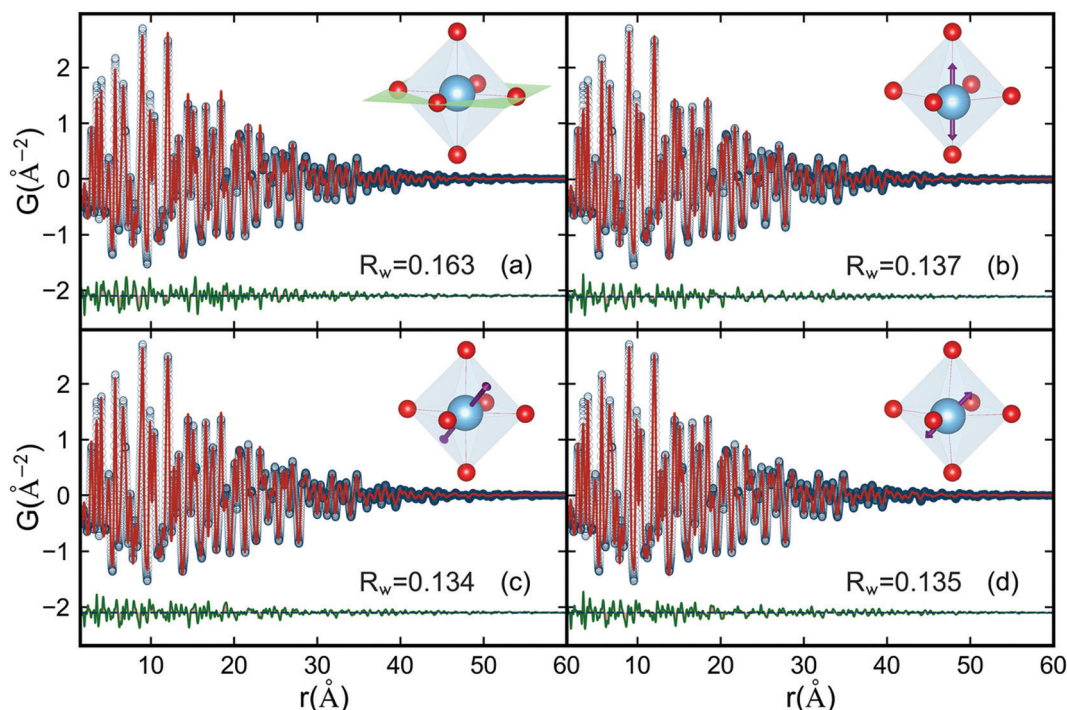


Fig. 2 Measured (open circles) and calculated (red solid lines) PDFs with difference curves shown offset below (green) for four candidate BaTiO₃ crystallographic phases fit to an experimental PDF from sub 10 nm nanocrystals (a) cubic ($Pm\bar{3}m$), (b) tetragonal ($P4/mmm$), (c) rhombohedral ($R3m$) and (d) orthorhombic ($Amm2$). In insets b–d, Ti-atoms (blue) are off-centered and the displacement modes are illustrated with vectors, while in (a), the Ti atom is centered and sits on a mirror plane perpendicular to the c -axis in the right panel.

Table 1 Refined parameters for the refinements of the various BTO phases to the data

	Centrosymmetric		Non-centrosymmetric		
	$Pm\bar{3}m$	$P4/mmm$	$P4mm$	$Amm2$	$R3m$
a (Å)	4.033	4.018	4.019	4.011	4.035
b (Å)	—	—	—	5.691	—
c (Å)	—	4.061	4.064	5.752	—
α (°)	—	—	—	—	89.582
c/a	—	1.011	1.011	—	—
Vol. (Å ³)	65.532	65.564	65.615	131.281	65.679
Ti (x,y,z)	$\left(\frac{1}{2}, \frac{1}{2}, \frac{1}{2}\right) LCXL$	$\left(\frac{1}{2}, \frac{1}{2}, \frac{1}{2}\right)$	$\left(\frac{1}{2}, \frac{1}{2}, 0.465\right)$	$\left(\frac{1}{2}, 0, 0.473\right)$	(0.478, 0.478, 0.478)
Ba- U_{iso} (Å ²)	0.009	0.007	0.008	0.007	0.008
Ti- U_{iso} (Å ²)	0.019	0.018	0.010	0.008	0.009
O- U_{iso} (Å ²)	0.027	0.026	0.025	0.025	0.023
SPD (Å)	59.190	61.402	62.607	63.316	67.218
R_w	0.163	0.159	0.137	0.135	0.134

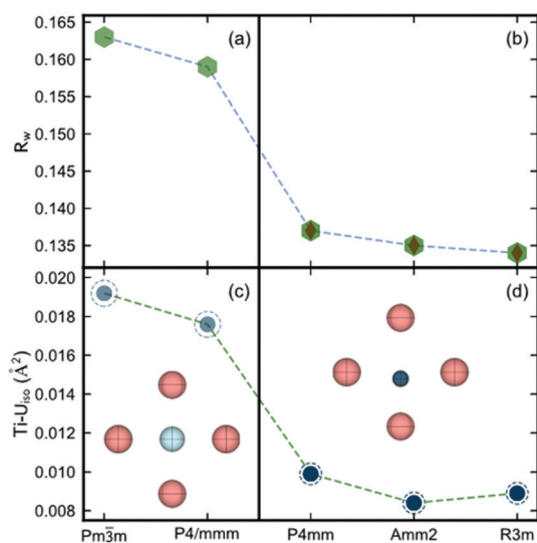


Fig. 3 The agreement factor R_w and atomic displacement parameters for Ti atoms for centrosymmetric (a and c) and non-centrosymmetric (b and d) candidate phases extracted from PDF refinements of 4.5 nm BaTiO₃ NPs. A full list of refined parameters for all five models is given in Table 1.

unambiguously among the non-centrosymmetric models themselves. However, we note that there is theoretical work⁵³ to support the off center distortion of Ti to a trigonal face of oxygens, based upon orbital overlap, consistent with the $R3m$ model, and indeed among the non-centrosymmetric models this had a slightly better agreement than the others despite having one fewer refinable parameter than the orthorhombic $Amm2$ model. Finally, we note that there is a significant amount of structural signal left over in the fit residuals (difference curves) shown in Fig. 2, even for the noncentrosymmetric models, which suggests the presence of other structural distortions away from the average structure that are not accounted for in the current models.

3.3 Raman scattering

Fig. 4 shows Raman spectra of the 4.5 nm BTO NPs in the temperature range of -150 to 400 °C. As the Raman spectra are

collected from the powder assembly, the peaks in Fig. 4 are considered in terms of quasi-phonons that are averaged over the directions of the net polarization of the individual particles.⁵⁴ Compared to the Raman spectra of coarse particles and ceramics,^{19,20} these spectra have broad features during all the temperatures, which indicates the crystal structure imperfection. Similar Raman spectra for very fine BaTiO₃ NPs were also reported.^{27,30,55} The bands at 304 and 725 cm⁻¹ in the spectra indicate the existence of a tetragonal phase in the sample. Compared to the Raman spectra of cubic BTO, two typical bands at 264 and 525 cm⁻¹ of 4.5 nm BTO NPs become very weak and broad, owing to the non-centrosymmetric regions induced by the displacement of the Ti in the TiO₆ octahedra.^{19,30,56,57}

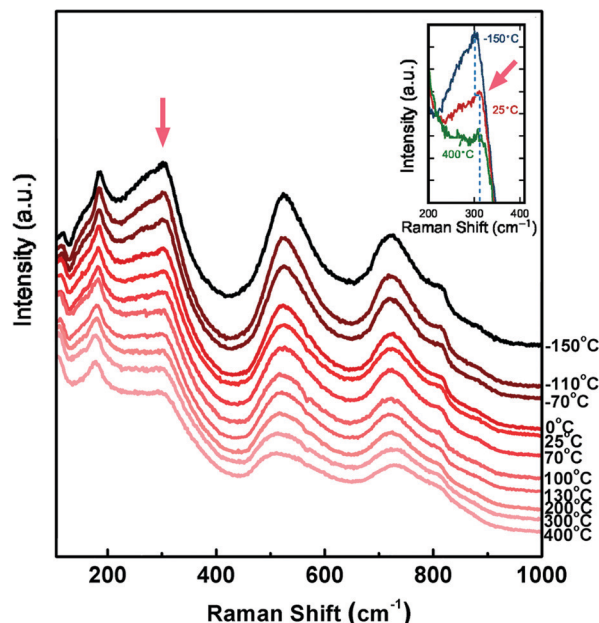


Fig. 4 Raman spectra at different temperatures for the 4.5 nm BaTiO₃ NPs. The locations of Raman modes are indicated at the top of the figure. The amplified figure for the tetragonal signature is inserted on the upper right.

With the increase of temperature, the spectra change gradually and the half-width of all lines increases. Normally, bulk BaTiO₃ materials undergo three phase transitions along with the increase of the temperature, which accompanies sharp band-shift steps or the appearance of new bands. Considering the bands at 304 cm⁻¹,⁵⁸ the frequency of this mode gradually increases about 10 cm⁻¹ wavenumbers from -70 to 25 °C, as amplified in the insertion, which indicates that a phase transition occurs in this region, and the phase transition is quite diffuse.^{20,59-61} Accordingly, the bands at 184 cm⁻¹ and 525 cm⁻¹ also show gradual shift to lower wavenumbers with the temperature increases. The changes in these modes occur in a wide temperature range with no sharp band-shift steps, which is probably caused by the phase coexistence during a wide temperature. This can be explained by the large number of surface defects that are induced by the organic ligands above the transition temperature.⁶² Similarly, the lack of a sharply defined phase transition was also observed on 26–45 nm BaTiO₃ NPs by Millicent *et al.* and other researchers.^{55,59} From the amplification in Fig. 4, although the peak broadening effect makes the two bands at 264 and 304 cm⁻¹ overlap seriously at high temperature, there is still a weak band remaining at 400 °C. Furthermore, the 725 cm⁻¹ bands persist over the entire temperature, which indicates the existence of tetragonal phase in the sample at relatively high temperatures. It can be ascribed to the surface ligand induced defects in the 4.5 nm BTO NPs which stabilize the tetragonal ferroelectric phase even at 400 °C. Therefore, Raman analyses confirm the diffuse phase transition of the 4.5 nm BTO NPs, and reveals the significant stable tetragonal ferroelectric phase at high temperatures.

3.4 Ferroelectric properties measurements

Although great efforts have been made in the characterization of the phase structure and crystal parameters of BTO nanoparticles, ferroelectric behaviour in such a small size has barely been reported.^{19,63,64} Taking advantage of the synthetic route, ferroelectric property measurements are taken on the BTO nanocrystalline thin film. It is noted that the BTO nanocrystalline thin film are characterized without further thermal treatment. Fig. 5 shows the high resolution (HR)-TEM image, scanning electron microscope (SEM) images of the BTO nanocrystalline thin film and photograph of the nanocrystal sol. The image has relatively high background intensity, but still shows clear lattice fringes of BTO, confirming the high crystallinity of the nanocrystals. Meanwhile, the quasi-spherical particles in this film are quite uniform with a particle size distribution in the range of 3–6 nm and an average diameter of 4.5 nm. The inserted photograph in Fig. 5c is the stable nanocrystal sol, which is used to fabricate thin film by spin-coating. Fig. 5b and c confirm the as-prepared nanocrystal film has a high quality with smooth surface and a thickness of 200–300 nm. The acquisition of dense nanocrystal film is a significant step in the investigation of size effect because it is very difficult to further decrease the grain size of bulk ceramics or characterize the ferroelectric behaviours directly on the fine BaTiO₃ nanopowders.

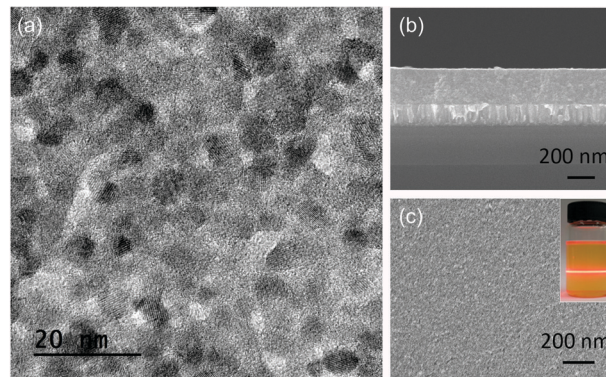


Fig. 5 (a) HR-TEM image of the BaTiO₃ nanocrystal film with particle sizes in the range of 3–6 nm and an average diameter of 4.5 nm. (b) Cross-sectional and (c) surface SEM images for the BaTiO₃ nanocrystal thin film. Inserted is the highly stable nanocrystal sol.

Anisotropic dielectrics possess a non-linear polarization. Its intensity can be expressed by power function of the electric field:

$$\vec{P}(t) = \chi^{(1)}\vec{E}(t) + \chi^{(2)}\vec{E}^2(t) + \chi^{(3)}\vec{E}^3(t) + \dots \quad (4)$$

In which $\chi^{(n)}$ is the polarization tensor. The high order terms are non-linear ones, which cannot be neglected under high electric field. Particularly the second order term $\chi^{(2)}$ is the polarization field that can generate frequency doubling, sum frequency, difference frequency and parametric oscillation.⁶⁵ Second-harmonic generation (SHG) is a nonlinear optical effect from the polarization at the doubled frequency, whose integral intensity is proportional to the spontaneous polarization in ferroelectrics.^{15,66,67} As shown in Fig. 6a, the illustrated light-path diagram is utilized to characterize the nonlinear response of the BaTiO₃ NPs. BaTiO₃ nanocrystal thin film with a relatively smooth surface is used to get enough reflected SHG signals. Before the measurement, the background SHG signal was collected on bare Pt-coated SiO₂/Si substrate to eliminate the errors caused by the light-path. As shown in Fig. S3 (ESI[†]), with the increase of the temperature, the background SHG signal increases, but maintains a relatively low value. The

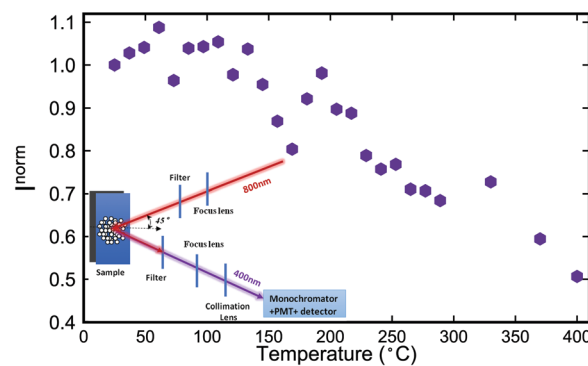


Fig. 6 Temperature dependence of the normalized SHG signal $I_{\text{norm}} = I(T)/(300 \text{ K})$ for the 4.5 nm BaTiO₃ NPs. The SHG light-path diagram is shown above.

quadratic dependence between the detected SHG signal and the laser power is shown in Fig. S4 (ESI[†]), which has a goodness-of-fit value R^2 reaching 0.995, confirming the second order nonlinear response of the nanocrystals. Fig. 6 shows that despite the intensity fluctuation that is caused by the reflected light, the frequency-doubled SHG signal gradually decreases with increase of the temperature, revealing an increasing structural symmetry of the nanocrystals. Similar curves were observed on BaTiO₃ powders by Pugachev *et al.*, instead of the normal polarization effect, they attribute it to polar nanoregions with local defects pinning the off-center Ti displacements.⁶⁶ Here the nanocrystals can be considered as separate nanoregions whose surfaces are pinned by the TEG ligand. In this way, the rather diffused phase transition behaviour is possibly affected by the surface coating. While this is inevitable for ultrafine nanocrystals obtained from the liquid phase synthetic route. To observe the SHG phenomenon intuitively, the BTO NPs is irradiated by an incident line with $\lambda = 1064$ nm, as detected by the THOR-LABS IRC3 plate, shown in Fig. S5a (ESI[†]). The photograph in Fig. S5b (ESI[†]) clearly shows that a green second harmonic signal (532 nm) is generated, which shows direct evidence that the 4.5 nm nanocrystals are non-centrosymmetric. Moreover, the diffuse decline of this nonlinear behaviour coincides well with the temperature-dependent Raman analysis, which provides irrefutable proof for the existence of non-centrosymmetric phases in these nanocrystals, and further confirms the diffuse phase transition characteristic of the nanocrystals.

PFM is used to verify the polarization ability of the ferroelectric BTO phases in the nanocrystal film. High-quality film is also needed for the electric polarization test, because the high writing voltage would collapse the incompact particles on the surface of the film and result in an anamorphic contrast. Here, Fig. 7c shows the topography image of the nanocrystal film with smooth, uniform and dense features, which is also the basis for the detection of ferroelectric response of the nanocrystals. As shown in Fig. 7a, the PFM measurements are conducted directly on the nanocrystal ensembles. By keeping the conductive tip fixed at the film surface and applying a bias voltage from -150 to $+150$ V on it, off-field piezoelectric responses are probed under V_{ac} , as shown in Fig. 7b. Despite of the noise level, a typical butterfly loop with the presence of a hysteresis and 180° phase switching show clearly that the polarizations are switchable in these nanocrystals, which indicates that stable ferroelectric switching behaviours are maintained at room temperature for the 4.5 nm BaTiO₃ nanocrystals. Although the value of the piezoelectric coefficient ($d_{33} = 3.5\text{--}5.0$ pm V⁻¹, due to the noise level) is significantly reduced from the bulk value ($d_{33} = 75$ pm V⁻¹; ref. 25), it is comparable to those obtained on 8 nm BaTiO₃ dense ceramic ($d_{33} = 20$ pm V⁻¹; ref. 48) and 10 nm individual nanocubes ($d_{33} = 1.55$ pm V⁻¹; ref. 16), which suggests superior preservation of piezoelectric properties in these 4.5 nm BaTiO₃ nanocrystals. Furthermore, to obtain the ferroelectric switching images, firstly a graphic pattern with voltage contrast from -40 to $+40$ V is applied on the conductive AFM tip that gently contacts the nanoparticles: the outer 2.0×2.0 μm square of the

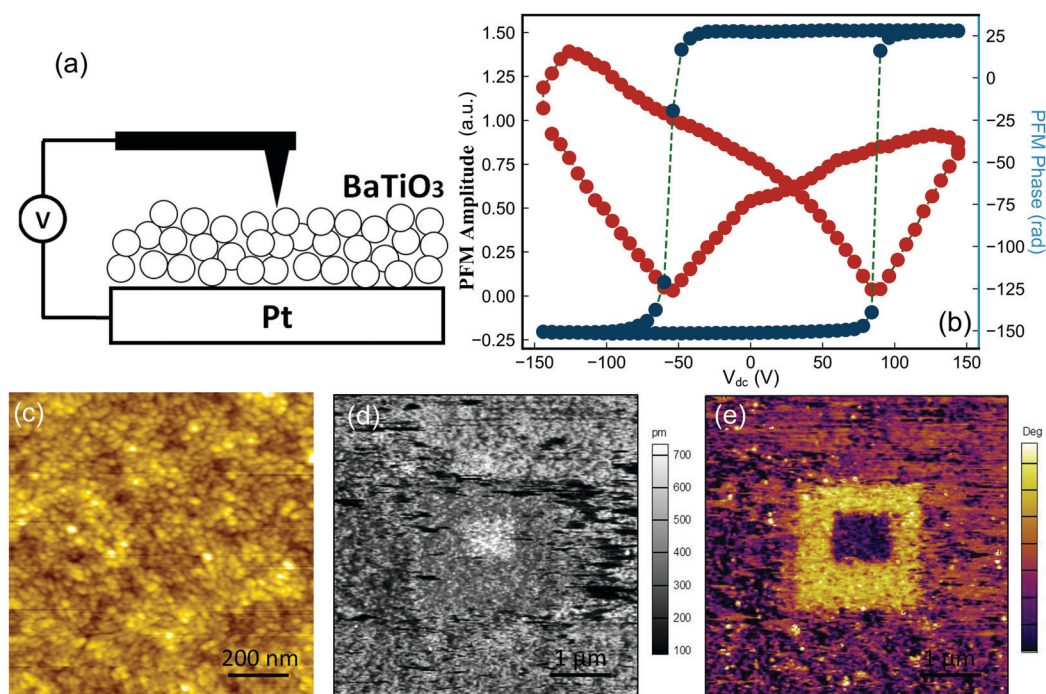


Fig. 7 (a) Schematic illustration of manipulating and probing the ferroelectric polarization of BaTiO₃ nanocrystals with PFM. (b) Off-field hysteresis loops separated in amplitude and phase, (c) AFM image, (d) ferroelectric polarization switching amplitude image (the inset one is amplitude image for the annealed sample) and (e) phase image of the BaTiO₃ nanocrystal film.

graphic pattern is written by a negative bias of -40 V and the inner square is reversed by a positive bias of $+40$ V. Then the resulting polarization is recorded with a lower reading V_{ac} of ± 5 V at the resonance frequency. Fig. 7d and e show the switched PFM amplitude and phase images of the nanocrystals after poling. Although the film is very thin, a high DC bias voltage is needed to pole the nanocrystals due to the partial voltage effect of the organic coatings. The residual organic matters also weaken the amplitude signal and result in a low-contrast but still discernible amplitude image. While the phase signal is independent of this and shows a clear polarization switching image with different voltages applied to the scanning tip. Combining with the SHG analyses, the ferroelectric polarization switching behaviour is speculated to be induced by reorientation of the spontaneous polarized individual particles under the field of the conducting tip. Thus the ferroelectric polarization switching imaging clearly demonstrates that the 4.5 nm BaTiO₃ nanocrystals possess ferroelectric properties in response to the applied external electric field and can be selectively written and read by PFM.

It is reported that charge injection effect and electrostatic interaction in some ionic conductors could also induce ferroelectric-like characteristics and lead to erroneous results.⁶⁸ In this method, the influence of organic surfactant, absorbed water, the surface and lattice hydroxyl groups, which might cause charge injection during the measurement, were carefully considered by comparing the sample with amorphous and annealed ones. The amorphous sample with the same organic residuals presents no polarization switching behaviour or hysteresis loop at different voltages (Fig. S6, ESI[†]), showing that the polarization in our sample could only be induced by the very fine nanoparticles. When most of the organic matters are gently removed at 400 °C without any grain growth, a more obvious amplitude image was obtained under a much lower voltage, shown in Fig. S7 (ESI[†]), which demonstrates that the organic residuals are more likely to restrain the detection of ferroelectricity in these nanoparticles. Therefore, although containing some organic molecules, the ferroelectric responses were confirmed to be induced by the polarization of the nanoparticles instead of the charge injection effect, and BaTiO₃ nanocrystals are successfully proved to still maintain ferroelectricity at an extremely small crystal size.

4. Conclusions

In summary, the presence of ferroelectricity in the 4.5 nm BaTiO₃ NPs is confirmed by phase structure analyses and direct ferroelectric response observation on SHG and PFM. PDF analysis reveals these nanocrystals possess a coherently non-centrosymmetric structure over the whole particle. When the particles are made into thin films they give a strong and measurable ferroelectric response at room temperature, with a remanent moment that is compared to bulk powders. With an increase in the temperature, they show a diffuse phase transition and gradually declined nonlinear optical effect. This result

is believed to be the closest achievement for the demonstration of the ferroelectric critical size of BaTiO₃ which not only promotes the critical ferroelectric limit research to a smaller value, but also opens up new opportunities for ultrafine BaTiO₃ NPs in future microelectronic applications, such as high density nonvolatile ferroelectric memories, ultrathin capacitors, *etc.* Moreover, due to the small particle size and high specific surface area, these nanocrystals are considered ideal fillers for ferroelectric nanocomposite devices that could offer a wide array of capabilities. We believe this research will provide theoretical basis for the nanosized ferroelectric device design in the near future.

Conflicts of interest

There are no conflicts to declare.

Acknowledgements

The work was supported by the National Natural Science Foundation of China (Grant No. 51972032, 51802023, 61774020 and 51802021), the Ministry of Sciences and Technology of China through National Basic Research Program of China (973 Program 2015CB654604), the National Key Research and Development Program of China (No. 2017YFB0406302), the Science and Technology Plan of Shenzhen City (Grant No. 201887776), Fund of IPOC BUPT (Grant No. IPOC2020ZT09) and the Key Area Research Plan of Guangdong (Grant No. 2019B010937001). We acknowledge the help from Beijing Synchrotron Radiation Facility in synchrotron XRD and Prof. Zhiyi Wei group for providing the laser line for the detection of frequency-doubled effect. Work in the Billinge group was supported by U.S. Department of Energy, Office of Science, Office of Basic Energy Sciences (DOE-BES) under contract no. DESC00112704. Banerjee acknowledges support from the National Defense Science and Engineering Graduate Fellowship (DOD-NDSEG) program. X-Ray PDF measurements were conducted on beamline 28-ID-2 of the National Synchrotron Light Source II, a U.S. Department of Energy (DOE) Office of Science User Facility operated for the DOE Office of Science by Brookhaven National Laboratory under Contract No. DE-SC0012704.

Notes and references

- 1 M. J. Pan and C. A. Randall, *IEEE Electr. Insul. Mag.*, 2010, **26**, 44.
- 2 H. Li, L. L. Ren, D. Ai, Z. B. Han, Y. Liu, B. Yao and Q. Wang, *InfoMat*, 2020, **2**(2), 389–400.
- 3 C. H. Ahn, K. M. Rabe and J.-M. Triscone, *Science*, 2004, **303**, 488.
- 4 J. M. Luo, E. Matios, H. Wang, X. Y. Tao and W. Y. Li, *InfoMat*, 2020, **2**(6), 1057–1076.
- 5 Y. Hao, X. Wang, K. Bi, J. Zhang, Y. Huang, L. Wu, P. Zhao, K. Xu, M. Lei and L. Li, *Nano Energy*, 2017, **31**, 49.

- 6 K. Bi, M. Bi, Y. Hao, W. Luo, Z. Cai, X. Wang and Y. Huang, *Nano Energy*, 2018, **51**, 513.
- 7 J. Junquera and P. Ghosez, *Nature*, 2003, **422**, 506.
- 8 K. Bi, D. Yang, J. Chen, Q. Wang, H. Wu, C. Lan and Y. Yang, *Photonics Res.*, 2019, **7**, 457.
- 9 S. Ramesh, B. A. Shutzberg, C. Huang, J. Gao and E. P. Giannelis, *IEEE Trans. Adv. Packag.*, 2003, **26**, 17.
- 10 H. Kishi, Y. Mizuno and H. Chazono, *Jpn. J. Appl. Phys.*, 2003, **42**, 1.
- 11 Y. Kobayashi, *et al.*, *Nat. Mater.*, 2012, **11**, 507.
- 12 S. Lin, X. Bai, H. Wang, H. Wang, J. Song, K. Huang, C. Wang, N. Wang, B. Li, M. Lei and H. Wu, *Adv. Mater.*, 2017, **29**, 1703238.
- 13 G. H. Kwei, S. J. L. Billinge, S.-W. Cheong and J. G. Sax-ton, *Ferroelectrics*, 1995, **164**, 57.
- 14 B. Bahrami, S. Mabrouk, N. Adhikari, H. Elbohy, A. Gurung, K. M. Reza, R. Pathak, A. H. Chowdhury, G. Saianand, W. J. Yue, J. T. Zai, X. F. Qian, M. Liang and Q. Q. Qiao, *InfoMat*, 2020, **2**(2), 409–423.
- 15 M. H. Frey and D. A. Payne, *Phys. Rev. B: Condens. Matter Mater. Phys.*, 1996, **54**, 3158.
- 16 R. E. Cohen, *Nature*, 1992, **358**, 136.
- 17 M. G. Stachiotti, *Appl. Phys. Lett.*, 2004, **84**, 251.
- 18 P. Gao, Z. Zhang, M. Li, R. Ishikawa, B. Feng, H.-J. Liu, Y.-L. Huang, N. Shibata, X. Ma and S. Chen, *Nat. Commun.*, 2017, **8**, 1.
- 19 X. Wang, X. Deng, H. Wen and L. Li, *Appl. Phys. Lett.*, 2006, **89**, 162902.
- 20 X. Deng, X. Wang, H. Wen, A. Kang, Z. Gui and L. Li, *J. Am. Ceram. Soc.*, 2006, **89**, 1059.
- 21 J. Zhu, W. Han, H. Zhang, Z. Yuan, X. Wang, L. Li and C. Jin, *J. Appl. Phys.*, 2012, **112**, 064110.
- 22 W. L. Zhong, Y. G. Wang, P. L. Zhang and B. D. Qu, *Phys. Rev. B: Condens. Matter Mater. Phys.*, 1994, **50**, 698.
- 23 K. Ishikawa and T. Uemori, *Phys. Rev. B: Condens. Matter Mater. Phys.*, 1999, **60**, 11841.
- 24 T. Hoshina, S. Wada, Y. Kuroiwa and T. Tsurumi, *Appl. Phys. Lett.*, 2008, **93**, 192914.
- 25 B.-D. Qu, W.-L. Zhong and P.-L. Zhang, *J. Phys.: Condens. Matter*, 1994, **6**, 1207.
- 26 M. D. Glinchuk, B. Y. Zaulychny and V. A. Stephanovich, *Phys. Solid State*, 2005, **47**, 1331.
- 27 Y. Shiratori, C. Pithan, J. Dornseiffer and R. Waser, *J. Raman Spectrosc.*, 2007, **38**, 1288.
- 28 T. Sun, X. Wang, H. Wang, X. Zhang, Z. Cheng, C. Q. Sun and L. Li, *J. Am. Ceram. Soc.*, 2010, **93**, 2571.
- 29 M. J. Polking, M.-G. Han, A. Yourdkhani, V. Petkov, C. F. Kisielowski, V. V. Volkov, Y. Zhu, G. Caruntu, A. Paul Alivisatos and R. Ramesh, *Nat. Mater.*, 2012, **11**, 700.
- 30 F. A. Rabuffetti and R. L. Brutchey, *J. Am. Chem. Soc.*, 2012, **134**, 9475.
- 31 V. Petkov, M. Gateshki, M. Niederberger and Y. Ren, *Chem. Mater.*, 2006, **18**, 814.
- 32 K. Page, T. Proffen, M. Niederberger and R. Seshadri, *Chem. Mater.*, 2010, **22**, 4386.
- 33 J. Chen, W. Du, J. Shi, M. Li, Y. Wang, Q. Zhang and X. Liu, *InfoMat*, 2020, **2**(1), 170–183.
- 34 Y. Hao, X. Wang and L. Li, *Nanoscale*, 2014, **6**, 7940.
- 35 P. J. Chupas, X. Qiu, J. C. Hanson, P. L. Lee, C. P. Grey and S. J. L. Billinge, *J. Appl. Crystallogr.*, 2003, **36**, 1342.
- 36 J. Kieffer and D. Karkoulis, *J. Phys.: Conf. Ser. SRI2012*, 2013.
- 37 C. J. Wright and X.-D. Zhou, *J. Synchrotron Radiat.*, 2017, **24**, 506.
- 38 P. Juhas, T. Davis, C. L. Farrow and S. J. L. Billinge, *J. Appl. Crystallogr.*, 2013, **46**, 560.
- 39 X. Yang, P. Juhas, C. Farrow and S. J. L. Billinge, arXiv 2015, 1402.3163.
- 40 C. L. Farrow and S. J. L. Billinge, *Acta Crystallogr., Sect. A: Found. Crystallogr.*, 2009, **65**, 232.
- 41 T. Egami and S. J. L. Billinge, *Underneath the Bragg peaks: structural analysis of complex materials*, Elsevier, Amsterdam, 2nd edn, 2012.
- 42 F. Bertolotti, L. Protesescu, M. V. Kovalenko, S. Yakunin, A. Cervellino, S. J. L. Billinge, M. W. Terban, J. S. Pedersen, N. Masciocchi and A. Guagliardi, *ACS Nano*, 2017, **11**, 3819.
- 43 A.-C. Dippel, K. M. Ø. Jensen, C. Tyrsted, M. Bremholm, E. D. Bøjesen, D. Saha, S. Birgisson, M. Christensen, S. J. L. Billinge and B. B. Iversen, *Acta Crystallogr., Sect. A: Found. Adv.*, 2016, **72**, 645.
- 44 A. N. Beecher, X. Yang, J. H. Palmer, A. L. LaGrassa, P. Juhas, S. J. L. Billinge and J. S. Owen, *J. Am. Chem. Soc.*, 2014, **136**, 10645.
- 45 S. Banerjee, C.-H. Liu, J. D. Lee, A. Kovyakh, V. Grasmik, O. Prymak, C. Koenigsman, H. Liu, L. Wang, A. M. M. Abeykoon, S. S. Wong, M. Epple, C. B. Murray and S. J. L. Billinge, *J. Phys. Chem. C*, 2018, **122**, 29498.
- 46 W. Cochran, *Adv. Phys.*, 1960, **9**, 387.
- 47 J. F. Scott, *Rev. Mod. Phys.*, 1974, **46**, 83.
- 48 G. H. Kwei, A. C. Lawson, S. J. L. Billinge and S. W. Cheong, *J. Phys. Chem.*, 1993, **97**, 2368.
- 49 G. H. Kwei, S. J. L. Billinge, S. W. Cheong and J. G. Saxton, *Ferroelectrics*, 1995, **164**, 57.
- 50 J. Lombardi, L. Yang, F. A. Pearsall, N. Farahmand, Z. Gai, S. J. L. Billinge and S. O'Brien, *Chem. Mater.*, 2019, **31**, 1318.
- 51 C. Shi, S. J. L. Billinge, E. Puma, S. H. Bang, N. J. H. Bean, J.-C. de Sugny, R. G. Gambia, R. C. Haskell, A. Hightower and T. C. Monson, *Phys. Rev. B*, 2018, **98**, 085421.
- 52 C. L. Farrow, P. Juhas, J. Liu, D. Bryndin, E. S. Bozin, J. Bloch, T. Proffen and S. J. L. Billinge, *J. Phys.: Condens. Matter*, 2007, **19**, 335219.
- 53 P. Ghosez, E. Cockayne, U. V. Waghmare and K. M. Rabe, *Phys. Rev. B: Condens. Matter Mater. Phys.*, 1999, **60**, 836.
- 54 I. Margaritescu, K. Datta and B. Mihailova, *J. Phys.: Condens. Matter*, 2018, **30**, 435401.
- 55 M. B. Smith, K. Page, T. Siegrist, P. L. Redmond, E. C. Walter, R. Seshadri, L. E. Brus and M. L. Steigerwald, *J. Am. Chem. Soc.*, 2008, **130**, 6955.
- 56 A. Scalabrin, A. S. Chaves, D. S. Shim and S. P. S. Porto, *Phys. Status Solidi B*, 1977, **79**, 731.

- 57 G. Busca, V. Buscaglia, M. Leoni and P. Nanni, *Chem. Mater.*, 1994, **6**, 955.
- 58 O. A. Maslova, F. V. Shirokov, Yu. I. Yuzyuk, M. El Marssi, M. Jain, N. Ortega and R. S. Katiyar, *J. Phys.: Condens. Matter*, 2014, **56**, 310.
- 59 Y. Li, Z. Liao, F. Fang, X. Wang, L. Li and J. Zhu, *Appl. Phys. Lett.*, 2014, **105**, 182901.
- 60 K. Kinoshita and A. Yamaji, *J. Appl. Phys.*, 1976, **47**, 371.
- 61 U. D. Venkateswaran, V. M. Naik and R. Naik, *Phys. Rev. B: Condens. Matter Mater. Phys.*, 1998, **58**, 14256.
- 62 E. Dul'kin, J. Petzelt, S. Kamba, E. Mojaev and M. Roth, *Appl. Phys. Lett.*, 2010, **97**, 032903.
- 63 N. Nuraje, K. Su, A. Haboosheh, J. Samson, E. P. Manning, N.-L. Yang and H. Matsui, *Adv. Mater.*, 2006, **18**, 807.
- 64 V. Bansal, P. Poddar, A. Ahmad and M. Sastry, *J. Am. Chem. Soc.*, 2006, **128**, 11958.
- 65 A. Zembrod, H. Puell and J. A. Giordmaine, *Opto-Electronics*, 1969, **1**, 64.
- 66 A. M. Pugachev, V. I. Kovalevskii, N. V. Surovtsev, S. Kojima, S. A. Prosandeev, I. P. Raevski and S. I. Raevskaya, *Phys. Rev. Lett.*, 2012, **108**, 247601.
- 67 S. K. Kurtz and T. T. Perry, *J. Appl. Phys.*, 1968, **39**, 379.
- 68 N. Balke, P. Maksymovych, S. Jesse, A. Herklotz, A. Tselev, C.-B. Eom, I. I. Kravchenko, P. Yu and S. V. Kalinin, *ACS Nano*, 2015, **9**, 6484.